J. Fluid Mech. (2003), *vol.* 483, *pp.* 315–342.
DOI: 10.1017/S002211200300421X Printed in the United Kingdom

Linear instability of a corrugated vortex sheet – a model for streak instability

By GENTA KAWAHARA[1], JAVIER JIMÉNEZ[2,3], MARKUS UHLMANN[2] AND ALFREDO PINELLI[2]

[1]Department of Aeronautics and Astronautics, Kyoto University, Kyoto 606-8501, Japan

[2]School of Aeronautics, Universidad Politécnica, 28040 Madrid, Spain

[3]Centre for Turbulence Research, Stanford University, Stanford, CA 94305, USA

(Received 15 August 2001 and in revised form 30 August 2002)

The linear inviscid instability of an infinitely thin vortex sheet, periodically corrugated with finite amplitude along the spanwise direction, is investigated analytically. Two types of corrugations are studied, one of which includes the presence of an impermeable wall. Exact eigensolutions are found in the limits of very long and of very short wavelengths. The intermediate-wavenumber range is explored by means of a second-order asymptotic series and by limited numerical integration. The sheets are unstable to both sinuous and varicose disturbances. The former are generally found to be more unstable, although the difference only appears for finite wavelengths. The effect of the corrugation is shown to be stabilizing, although in the wall-bounded sheet the effect is partly compensated by the increase in the distance from the wall. The controlling parameter in that case appears to be the minimum separation from the sheet valley to the wall. The instability is traced to a pair of oblique Kelvin–Helmholtz waves in the flat-sheet limit, but the eigenfunctions change character both as the corrugation is made sharper and as the wall is approached, becoming localized near the crests and valleys of the corrugation. The study is motivated by the desire to understand the behaviour of lifted low-speed streaks in wall-bounded flows, and it is shown that the spatial structure of the fundamental sinuous eigenmode is remarkably similar to previously known three-dimensional nonlinear equilibrium solutions in both plane Couette and Poiseuille flows.

1. Introduction

An aspect of wall turbulence that has recently been the subject of much attention is the presence of self-sustaining coherent structures that appear to control the near-wall flow dynamics. The dominant structures are elongated streamwise velocity streaks and longitudinal vortices. The low- and high-velocity streaks are arranged alternately in the spanwise direction (Kline *et al.* 1967), while shorter streamwise vortices of both signs are typically staggered alongside them (Stretch 1990; Jiménez & Moin 1991; Jeong *et al.* 1997).

It is generally believed that streaks and vortices are involved in a nonlinear self-sustaining cycle that maintains near-wall turbulence (Jiménez 1994; Hamilton, Kim & Waleffe 1995; Waleffe 1997; Kawahara & Kida 2001). A collection of papers developing this point of view has been edited by Panton (1997).

It has long been recognized that the streaks are generated by cross-flow advection of the gradient of the streamwise velocity by the streamwise vortices (Kline *et al.* 1967;

Bakewell & Lumley 1967). Low-speed fluid is lifted away from the wall, producing a low-speed streak, while high-speed fluid is pushed towards the wall, creating a high-speed one. This process leads to an overall increase of mean wall shear, and is the essential ingredient in the generation of turbulent wall drag (Orlandi & Jiménez 1994). Much effort has, therefore, been devoted to elucidating the dynamics of streamwise vortices, with a view to understanding and controlling near-wall turbulence, but there is still no general agreement about the mechanisms by which they are produced or reproduced.

In their direct numerical simulations of highly constrained plane Poiseuille turbulence, Jiménez & Moin (1991) examined the dynamics of near-wall structures in detail. They minimized the streamwise and spanwise dimensions of a computational periodic box to the size in which turbulence was just sustained, and obtained a flow consisting of an array of identical structures. They observed that, when the low-speed streak bends in the spanwise direction, the flow becomes highly three-dimensional, and new streamwise vortices are generated by vortex stretching. Although other plausible mechanics for vortex generation have been proposed, such as the effect of the outer flow (Sreenivasan 1988), or the reaction of the no-slip wall (Brooke & Hanratty 1993), a recent study by Jiménez & Pinelli (1999) demonstrates that vortex generation is predominantly associated with the presence of streaks in the buffer layer.

Hamilton *et al.* (1995) used the same technique as Jiménez & Moin (1991) to investigate the generation mechanism of streamwise vortices in a minimal plane Couette flow. Their most important finding, from the point of view of the present paper, was that a purely two-dimensional flow containing only straight streaks in addition to the mean flow is linearly unstable. The instability takes the form of a sinuous (bending) disturbance of the streak. The subsequent nonlinear three-dimensionalization creates streamwise vortices which in turn regenerate the streaks, completing the self-sustaining cycle.

This finding suggests that the sinuous instability of a straight streak is at the origin of the generation of streamwise vortices in the buffer layer (Waleffe 1997). The vortices themselves seem to be necessary only for preventing streaks from being damped by viscous diffusion (Itano & Toh 2001).

There is a substantial body of work on the linear instability of model streaks with smooth velocity fields, much of it oriented towards the prediction of bypass transition in boundary layers. Waleffe (1995, 1997) and Waleffe & Kim (1997) numerically analysed one such model in a low-Reynolds-number plane Couette flow, and conjectured that the instability originates from the inflectional layers of wall-normal vorticity which separate the low- from the high-speed streaks. This wake-like instability had first been proposed by Swearingen & Blackwelder (1987), who studied the streaky structures caused by Görtler vortices in a boundary layer. The associated inviscid stability problem was first considered by Hall & Horseman (1991), who concluded that the breakdown was instead most probably due to the horizontal layer of enhanced spanwise vorticity above the streak. Later work has shown that both mechanisms can be important depending on the parameters of the base flow, and that different modes can be qualitatively associated with different locations on the periphery of the streak. For a recent summary see Reddy *et al.* (1998). The vortices generated by this instability mechanism should be normal to a wall, but they would be tilted and stretched in the streamwise direction under the action of the mean shear (Jiménez 1994).

Schoppa & Hussain (1997, 1998), on the other hand, investigated the instability of a model streak in a minimal plane Poiseuille flow, and showed that, although their base

flow was strictly unidirectional, the unstable sinuous eigenstructures appearing in the linear stage of the growth were already dominated by layers of streamwise vorticity. They noted the similarity of those structures with the oblique modes observed after roll pairing in plane mixing layers, and conjectured that the instability of the streaks could be linked to that process, rather than to the wake-like mechanism mentioned above (Schoppa, Hussain & Metcalfe 1995). This group was also the first to explicitly propose the modelling of the buffer-layer streaks by a corrugated shear layer and to confirm numerically the similarity of the eigenfunctions in the three cases (Schoppa 2000; Schoppa & Hussain 2002). They introduced a corrugated coordinate system referenced to the base-flow vortex lines to demonstrate the vorticity dynamics in the instability, as well as in the transient growth of linear perturbations.

Since the various mechanisms discussed above are in principle different, one of the purposes of the present paper is to clarify the origin of the streak instability by analysing a simple flow whose behaviour can be studied as thoroughly as possible. Such studies are useful because it cannot be automatically assumed that the smooth models used for the streaks in the studies mentioned above are necessarily realistic, and it is not known how their details influence their stability. This became apparent, for example, in the analysis by Kawahara *et al.* (1998) of a smooth model very similar to the one used by Schoppa & Hussain (1997). They found at least three different instability mechanisms that could be distinguished by discontinuities in the neutral surface, and which were associated with different ranges of the spanwise wavelength.

Consider for example the problem of whether a most unstable wavelength exists. In a plane vorticity layer the only relevant length is the layer thickness, and it can safely be predicted that the perturbation wavelength should be normalized with it. In the present case two additional length scales are the spanwise wavelength and of the distance to the wall. All the analyses mentioned above were done numerically for particular families of continuous velocity profiles in which those three scales could not easily be varied independently. Schoppa & Hussain (2002), for example, numerically explored the dependence of the growth rate on the longitudinal wavelength of the perturbations and on the amplitude of the streak but, while they found an optimal wavelength for a given amplitude, they only then explored the effect of that amplitude for that particular wavelength. They parameterized their velocity profiles in terms of a particular elevation angle of the vortex surfaces, but it is difficult in this kind of analyses to distinguish whether the optimal wavelength is a function of the curvature of the isosurfaces, of their lifting above the wall, or even of the ratio of any of these quantities with the thickness of the shear layer. Analytic solutions do not sufer from these limitations and, while it is clear that they can also be only found for particular velocity distributions, they easily allow questions such as what is the effect of curvature or of lifting to be answered.

All the instability mechanisms mentioned above are inflectional, and thus most probably independent of the effect of viscosity (see Schoppa & Hussain 1997). We shall therefore only analyse inviscid models, and in particular we shall represent the streak by an infinitely thin vortex sheet, corrugated along the spanwise direction and adjacent to a slip wall. The simplicity of the model allows us to obtain full analytical expressions for the eigensolutions, at least in the limits of long or short waves, and to separate the effect of sheet curvature from those of wall distance. The analysis is done in two stages. The technique is first developed for a free sheet in the absence of a wall. Only later is the influence of the wall included.

This approximation restricts the practical applicability of our results to the case of long waves. This will be the limit studied in the paper, but it is also the case observed

in experiments. It is well known that vortex sheets are ill-posed, in the sense that the most unstable wavelengths are the shortest ones, with growth rates that become unbounded in that limit and which lead to the finite-time formation of singularities (Moore 1979; Cowley, Baker & Tanveer 1999). We will see that the linear result on the high-wavenumber limit of the instability also holds for the corrugated sheets, so that we will not be able to speak about maximum growth rates. Those are determined in real flows by the thickness of the vortex layer, or by viscosity.

It should be noted that, although our motivation is primarily to understand the behaviour of wall flows, the corrugated vortex sheet is itself of some importance, having for example been used by Lasheras & Choi (1988) to inject streamwise vorticity in free shear layers. That effect was later used commercially to control large-scale mixing and noise generation. We are not aware of any analysis of the stability of that flow, although the simpler case of the non-uniform planar layer was analysed first by Hocking (1964) in the vortex-sheet approximation, and more recently by Saxena, Leibovich & Berkooz (1999) in an inviscid smooth one. Both find an enhancement of the instability, although it will be seen below that we find the effect of the corrugation to be stabilizing.

There are in fact relatively few examples of fully two-dimensional base flows whose stability characteristics are known, and the final goal of our paper is to add to the understanding of how they differ from the more classical one-dimensional ones, particularly regarding the generation of streamwise vorticity.

The organization of the paper is as follows. In § 2 we derive the linearized equations for the perturbations of the corrugated vortex sheet, and introduce the conformal mapping used for the definition of the geometry. The asymptotic solution of the problem in the limit of very small wavenumbers is developed in § 3, both for sinuous and for varicose perturbations. The influence of the impermeable wall is considered in § 3.3. The higher-order corrections to the eigenvalues are derived in § 4, which also briefly discusses some numerical results for the instability at intermediate wavenumbers. The short-wavelength limit is analysed in Appendix A. Finally, in § 5, we compare the linear eigensolutions with two previously published three-dimensional nonlinear equilibrium solutions in Couette and Poiseuille flows, and offer conclusions.

2. Formulation

We shall consider an infinitely thin and smooth vortex sheet defined by $S(y, z) = 0$ (figure 1). The sheet is infinite and periodically corrugated with finite amplitude and wavelength 2π in the spanwise direction z, and is uniform in the streamwise direction x. The velocity is $U\boldsymbol{e}_x$, where $U = \pm 1$ respectively above and below the sheet, and $\boldsymbol{e}_x$ is the unit vector in the x-direction. Vorticity is confined to the sheet, and its x-component is initially null. Such sheets are steady solutions of the Euler equation, and may be regarded as the simplest models for the streaky structure observed in shear flows, although they are different from the case of interest for turbulent transition, in which the flow without streaks, i.e. without corrugation, is known to be stable.

2.1. *Basic equations*

Consider a general infinitesimal disturbance both to the location of the sheet and to its circulation density. We will only consider perturbations in which the vorticity remains confined to the perturbed sheet, so that there exists a velocity potential $\phi(x, y, z, t)$ such that the disturbance velocity $\boldsymbol{v}(x, y, z, t)$ is expressed as $\boldsymbol{v} = \nabla\phi$

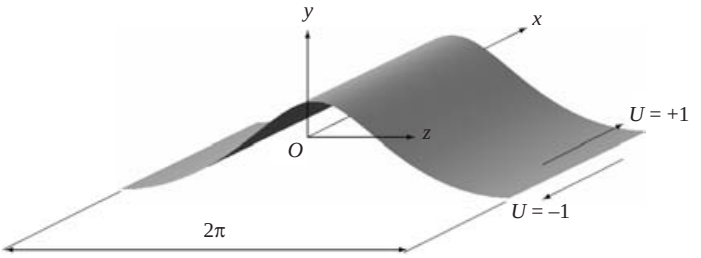

FIGURE 1. The configuration of a corrugated vortex sheet. The streamwise (x) component of the velocity is ± 1 above and below the sheet. One period of the infinite sheet is shown in the z-direction.

outside the sheet, and

$$\nabla^2 \phi = 0. \tag{2.1}$$

If the disturbance decays as $y \to \pm\infty$, the linearized Bernoulli equation yields

$$\left(\frac{\partial}{\partial t} + U\frac{\partial}{\partial x}\right)\phi + p = 0, \tag{2.2}$$

where p is the pressure. Defining the perturbed vortex sheet by

$$S(y, z) + s(x, y, z, t) = 0, \tag{2.3}$$

the function s must satisfy the linearized kinematic condition

$$\left(\frac{\partial}{\partial t} + U\frac{\partial}{\partial x}\right)s + \left(\frac{\partial \phi}{\partial y}\frac{\partial}{\partial y} + \frac{\partial \phi}{\partial z}\frac{\partial}{\partial z}\right)S = 0 \quad \text{on } S(y, z) = 0, \tag{2.4}$$

because the sheet is a material surface.

We next write ϕ as a normal mode,

$$\phi(x, y, z, t) = \mathrm{Re}\{\widetilde{\phi}(y, z)\, \mathrm{e}^{\mathrm{i}\alpha(x-ct)}\}, \tag{2.5}$$

where α is a real wavenumber and c is a complex phase velocity. Substituting this expression, and similar ones for p and s, into (2.1), (2.2) and (2.4), we obtain

$$\left(\frac{\partial^2}{\partial y^2} + \frac{\partial^2}{\partial z^2}\right)\widetilde{\phi} - \alpha^2 \widetilde{\phi} = 0, \tag{2.6}$$

$$\mathrm{i}\alpha(U - c)\widetilde{\phi} + \widetilde{p} = 0, \tag{2.7}$$

$$\mathrm{i}\alpha(U - c)\widetilde{s} + \left(\frac{\partial \widetilde{\phi}}{\partial y}\frac{\partial}{\partial y} + \frac{\partial \widetilde{\phi}}{\partial z}\frac{\partial}{\partial z}\right)S = 0 \quad \text{on } S(y, z) = 0. \tag{2.8}$$

2.2. *Conformal mapping*

We introduce now the complex variable $\chi = y + \mathrm{i}z$ in the cross-flow plane, and restrict our analysis to sheets whose corrugation can be defined in terms of simple conformal maps. Consider for example the mapping, $\zeta = \eta + \mathrm{i}\xi \leftrightarrow \chi$, given by

$$\chi = 2\log\left(\cos\tfrac{1}{2}\zeta\right), \quad \zeta = 2\arccos\left(\mathrm{e}^{\chi/2}\right), \tag{2.9}$$

which maps the infinite periodic strip $y \in (-\infty, \infty)$, $z \in (-\pi, \pi)$ into the semi-infinite one $\xi \in (0, \infty)$, $\eta \in (-\pi, \pi)$. We define the undisturbed vortex sheet as the

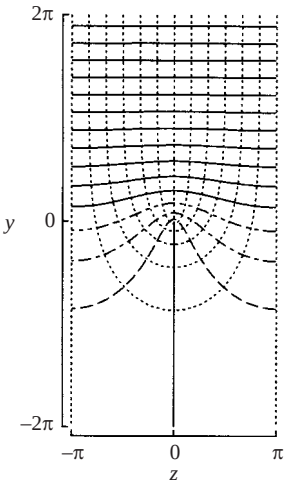

FIGURE 2. Iso-contours of ξ and η defined by the conformal mapping (2.9). One period is shown in the z-direction. The dotted lines are η-contours. The dotted vertical lines at $z = \pm\pi$ are $\eta = \mp\pi$. Otherwise, from right to left, $\eta = k\pi/6$; $k = -5(1)5$. All the other lines are ξ-contours. The solid vertical line at $z = 0$, $y \leqslant 0$ is $\xi = 0$. – – – –, $\xi = \frac{1}{6}\pi$; —·— , $\xi = \frac{1}{3}\pi$; —··—, $\xi = \frac{1}{2}\pi$. These three values are used for the definition of the sheets in figure 3. The rest of the solid isolines are $\xi = k\pi/6$, $k = 4(1)14$, moving upwards.

isosurface

$$S(y, z) \equiv \xi - \xi_0 = 0, \tag{2.10}$$

where $\xi_0 > 0$ is a constant which parameterizes the depth of the corrugation.

Figure 2 shows iso-contours of ξ and η in the (y, z)-plane. The ξ-contours, which represent possible positions of the sheet, become flatter for $\xi \gg 1$, with $y \approx \xi$ and $z \approx -\eta$, so that $y \to \infty$ as $\xi \to \infty$. For smaller ξ the corrugation becomes deeper and the crests sharper. The limit $y \to -\infty$ is mapped into the points $\zeta = (2k+1)\pi$, where, and throughout the paper, k stands for an arbitrary integer.

The Jacobian $J(\xi, \eta)$ of (2.9) is

$$J \equiv \frac{\partial(\eta, \xi)}{\partial(y, z)} = \left|\cot \tfrac{1}{2}\zeta\right|^2 = \frac{\cosh\xi + \cos\eta}{\cosh\xi - \cos\eta}, \tag{2.11}$$

and the mapping is singular both at $y \to -\infty$, $\zeta \to (2k+1)\pi$, where $J \to 0$, and at $(y, z) \to (0, -2k\pi)$, $\zeta \to 2k\pi$, where $J \to \infty$. The Fourier expansion of the reciprocal of J will be needed later, and can be written as

$$J^{-1} = \sum_{m=0}^{\infty} j_m(\xi) \cos m\eta, \tag{2.12}$$

with the Fourier coefficients

$$j_0 = 1 + 2\mathrm{e}^{-\xi}/\sinh\xi, \quad j_m = 4(-1)^m \mathrm{e}^{-m\xi}/\tanh\xi \ \ (m \geqslant 1). \tag{2.13}$$

By expressing (2.6) and (2.8) in the independent variables ξ and η we obtain

$$\left(\frac{\partial^2}{\partial\xi^2} + \frac{\partial^2}{\partial\eta^2}\right)\widetilde{\phi} - \alpha^2 J^{-1}\widetilde{\phi} = 0, \tag{2.14}$$

$$-\mathrm{i}\alpha(U-c)\widetilde{\xi}+J\frac{\partial\widetilde{\phi}}{\partial\xi}=0 \quad \text{on } \xi=\xi_0, \tag{2.15}$$

where we have defined $\widetilde{\xi}(\eta)=-\widetilde{s}(y,z)$, and rewritten the perturbed sheet (2.3) as

$$\xi=\xi_0+\mathrm{Re}\{\widetilde{\xi}(\eta)\,\mathrm{e}^{\mathrm{i}\alpha(x-ct)}\}. \tag{2.16}$$

To obtain the matching conditions across the sheet, we express the velocity potential above and below the vortex sheet as

$$\widetilde{\phi}(\xi,\eta)=\begin{cases}\widetilde{\phi}^{+}(\xi,\eta) & (\xi>\xi_0)\\ \widetilde{\phi}^{-}(\xi,\eta) & (\xi<\xi_0).\end{cases} \tag{2.17}$$

The continuity of the pressure in (2.7) yields

$$(1-c)\widetilde{\phi}^{+}+(1+c)\widetilde{\phi}^{-}=0 \quad \text{on } \xi=\xi_0, \tag{2.18}$$

while the consistency of the kinematic condition (2.15) on the upper and lower surfaces of the sheet results in

$$(1+c)\frac{\partial\widetilde{\phi}^{+}}{\partial\xi}+(1-c)\frac{\partial\widetilde{\phi}^{-}}{\partial\xi}=0 \quad \text{on } \xi=\xi_0. \tag{2.19}$$

Equations (2.14), (2.18) and (2.19) define the eigenvalue problem for c.

2.3. *Streamwise vorticity*

It is important to realize that Squire's theorem cannot be used in three-dimensional situations, such as the present one, and that the eigenfunctions would in general be oblique and contain streamwise vorticity. The vorticity $\boldsymbol{\omega}$ can be expressed as

$$\boldsymbol{\omega}=\boldsymbol{\Omega}\delta(l), \tag{2.20}$$

where $\boldsymbol{\Omega}$ denotes the circulation density vector, which is parallel to the sheet, l is the distance along a unit vector $\boldsymbol{l}$ perpendicular to the sheet, and $\delta(l)$ is the Dirac delta function. The circulation density is (see Saffman 1992, § 2.2)

$$\boldsymbol{\Omega}=\boldsymbol{l}\times[\nabla\phi], \tag{2.21}$$

where we have introduced the notation $[\cdot]$ for the jump of a quantity across the sheet,

$$[\nabla\phi]=\nabla\phi^{+}|_{\xi=\xi_0}-\nabla\phi^{-}|_{\xi=\xi_0}. \tag{2.22}$$

The linearized expression of the streamwise component Ω_x of the circulation density, which gives the jump of the tangential velocity in the (y,z)-plane, is then

$$\Omega_x=-J^{1/2}|_{\xi=\xi_0}\,\mathrm{Re}\left\{\left[\frac{\partial\widetilde{\phi}}{\partial\eta}\right]\mathrm{e}^{\mathrm{i}\alpha(x-ct)}\right\}. \tag{2.23}$$

3. The long-wavelength limit

The structures observed in wall-bounded flows are long, with streamwise wavelengths of the order of three or four times the streak spacing (Jiménez & Moin 1991; Schoppa & Hussain 1997), and it was shown that those wavelengths are

comparable to the streamwise wavelength for the most unstable viscous eigenfunctions of model streaks (Kawahara *et al.* 1998; Schoppa 2000; Schoppa & Hussain 2002). We can expect that any shorter eigenfunctions which appear in the inviscid analysis will be strongly damped by viscosity.

Guided by these considerations we shall first study the long-wave limit of the eigenvalue problem, $\alpha \ll 1$, and look for asymptotic solutions of the form

$$\widetilde{\phi}^{\pm} = \alpha\big(\widetilde{\phi}_0^{\pm}(\xi, \eta) + \alpha^2\widetilde{\phi}_2^{\pm}(\xi, \eta) + \cdots\big), \tag{3.1}$$

$$c = c_0 + \alpha^2 c_2 + \cdots, \tag{3.2}$$

with the sheet located at

$$\widetilde{\xi} = \widetilde{\xi}_0(\eta) + \alpha^2\widetilde{\xi}_2(\eta) + \cdots. \tag{3.3}$$

A possible solution with $c = O(\alpha^{-1})$ and $\widetilde{\phi} = O(1)$ is trivial and has not been included in the expansions. Indeed, if $c_{-1} = 0$ it follows from (2.15) that $\partial\widetilde{\phi}/\partial\xi = 0$ on the upper and the lower surfaces of the vortex sheet, so that $\widetilde{\phi}$ is identically zero under the conditions that $\widetilde{\phi} \to 0$ at $y \to \pm\infty$. On the other hand, if $c_{-1} \neq 0$, the leading orders of (2.18) and (2.19) imply that both $\widetilde{\phi}$ and $\partial\widetilde{\phi}/\partial\xi$ are continuous across the sheet, which again means that $\widetilde{\phi}$ is identically zero.

Substituting (3.1) and (3.2) into (2.14), (2.18) and (2.19), and separating orders, we have to $O(1)$,

$$\left(\frac{\partial^2}{\partial\xi^2} + \frac{\partial^2}{\partial\eta^2}\right)\widetilde{\phi}_0^{\pm} = 0, \tag{3.4}$$

$$(1 - c_0)\widetilde{\phi}_0^{+} + (1 + c_0)\widetilde{\phi}_0^{-} = 0 \quad \text{on } \xi = \xi_0, \tag{3.5}$$

$$(1 + c_0)\frac{\partial\widetilde{\phi}_0^{+}}{\partial\xi} + (1 - c_0)\frac{\partial\widetilde{\phi}_0^{-}}{\partial\xi} = 0 \quad \text{on } \xi = \xi_0, \tag{3.6}$$

and to $O(\alpha^2)$,

$$\left(\frac{\partial^2}{\partial\xi^2} + \frac{\partial^2}{\partial\eta^2}\right)\widetilde{\phi}_2^{\pm} = J^{-1}\widetilde{\phi}_0^{\pm}, \tag{3.7}$$

$$(1 - c_0)\widetilde{\phi}_2^{+} + (1 + c_0)\widetilde{\phi}_2^{-} = c_2[\widetilde{\phi}_0] \quad \text{on } \xi = \xi_0, \tag{3.8}$$

$$(1 + c_0)\frac{\partial\widetilde{\phi}_2^{+}}{\partial\xi} + (1 - c_0)\frac{\partial\widetilde{\phi}_2^{-}}{\partial\xi} = -c_2\left[\frac{\partial\widetilde{\phi}_0}{\partial\xi}\right] \quad \text{on } \xi = \xi_0. \tag{3.9}$$

We shall study first the leading-order problem (3.4)–(3.6).

3.1. *Leading order*

It follows from the symmetry of the base flow that the sinuous modes, for which $\widetilde{\phi}$ is odd with respect to $\eta = k\pi$ ($z = k\pi$), can be treated independently from the varicose ones for which $\widetilde{\phi}$ is even. The former are probably related to the observations of wavy streaks mentioned above, while the latter should rather be connected with the generation of the hairpin vortices described for example by Acarlar & Smith (1987) and Asai, Minagawa & Nishioka (2002). Consider first the sinuous case, for which the velocity potential may be written in terms of normal modes as

$$\widetilde{\phi}_0^{\pm} = \widetilde{\phi}_{0,n}^{\pm}(\xi)\sin n\eta \quad (n = 1, 2, 3, \ldots), \tag{3.10}$$

but note that these are not pure spanwise modes in physical space (i.e. $\sin n\eta \neq \sin nz$). Substitution of (3.10) into (3.4) leads to

$$\left(\frac{\mathrm{d}^2}{\mathrm{d}\xi^2} - n^2\right)\widetilde{\phi}^{\pm}_{0,n} = 0, \tag{3.11}$$

which has solutions

$$\widetilde{\phi}^{\pm}_{0,n} = A\,\mathrm{e}^{+n\xi} + B\,\mathrm{e}^{-n\xi}, \tag{3.12}$$

where A and B are arbitrary constants.

Since $\widetilde{\phi}^{\pm}_0$ are analytic functions of ζ, the modal 'complex velocity' in the (y, z)-plane is given by

$$\widetilde{v} - \mathrm{i}\widetilde{w} = \frac{\mathrm{d}\zeta}{\mathrm{d}\chi}\left(\frac{\partial\widetilde{\phi}^{\pm}_0}{\partial\eta} - \mathrm{i}\frac{\partial\widetilde{\phi}^{\pm}_0}{\partial\xi}\right) = -\cot\tfrac{1}{2}\zeta\left(n\widetilde{\phi}^{\pm}_{0,n}\cos n\eta - \mathrm{i}\frac{\mathrm{d}\widetilde{\phi}^{\pm}_{0,n}}{\mathrm{d}\xi}\sin n\eta\right). \tag{3.13}$$

Thus, in order for the disturbance velocity to be regular at $\zeta = 2k\pi$ we must have

$$\widetilde{\phi}^{-}_{0,n}(0) = 0. \tag{3.14}$$

It then follows from (3.13) and (3.14) that the velocity decays as $y \to -\infty$, i.e. $\zeta \to (2k+1)\,\pi$, if $\mathrm{d}\widetilde{\phi}^{-}_{0,n}/\mathrm{d}\xi$ is finite at $\xi \to 0$. On the other hand, for the velocity to decay at $y \to \infty$, i.e. $\xi \to \infty$, we need

$$\widetilde{\phi}^{+}_{0,n}(\infty) = 0. \tag{3.15}$$

We therefore take the velocity potential below and above the vortex sheet as

$$\widetilde{\phi}^{-}_{0,n} = A_-\sinh n\xi, \quad \widetilde{\phi}^{+}_{0,n} = B_+\,\mathrm{e}^{-n\xi}. \tag{3.16}$$

Substituting (3.16) into the matching conditions (3.5) and (3.6), we obtain

$$(1-c_0)\,\mathrm{e}^{-n\xi_0}\,B_+ + (1+c_0)\sinh n\xi_0\,A_- = 0, \tag{3.17}$$

$$-(1+c_0)\,\mathrm{e}^{-n\xi_0}\,B_+ + (1-c_0)\cosh n\xi_0\,A_- = 0, \tag{3.18}$$

which determine the leading-order eigenvalues

$$c_0 = \mathrm{e}^{-2n\xi_0} \pm \mathrm{i}\left(1 - \mathrm{e}^{-4n\xi_0}\right)^{1/2}, \tag{3.19}$$

and the corresponding eigenfunctions

$$\widetilde{\phi}^{-}_{0,n} = C(1-c_0)\,\mathrm{e}^{-n\xi_0}\sinh n\xi, \quad \widetilde{\phi}^{+}_{0,n} = -C(1+c_0)\,\mathrm{e}^{-n\xi}\sinh n\xi_0, \tag{3.20}$$

where the constant C is arbitrary.

The varicose mode can be treated in a similar way. The potential has the form

$$\widetilde{\phi}_0 = \begin{cases} \widetilde{\phi}^{+}_{0,n}(\xi)\cos n\eta + (-1)^n\dfrac{1+c_0}{1-c_0}\widetilde{\phi}^{-}_{0,n}(0) & (\xi > \xi_0) \\ \widetilde{\phi}^{-}_{0,n}(\xi)\cos n\eta - (-1)^n\widetilde{\phi}^{-}_{0,n}(0) & (\xi < \xi_0) \end{cases} \qquad (n = 1, 2, 3, \ldots), \tag{3.21}$$

which should vanish as $\zeta \to (2k+1)\pi$, i.e. $y \to -\infty$, so that $J^{-1}\widetilde{\phi}$ remains finite in (2.14). The resulting eigenvalues and eigenfunctions are

$$c_0 = -\mathrm{e}^{-2n\xi_0} \pm \mathrm{i}\left(1 - \mathrm{e}^{-4n\xi_0}\right)^{1/2}, \tag{3.22}$$

and

$$\widetilde{\phi}^{-}_{0,n} = C(1-c_0)\,\mathrm{e}^{-n\xi_0}\cosh n\xi, \quad \widetilde{\phi}^{+}_{0,n} = -C(1+c_0)\,\mathrm{e}^{-n\xi}\cosh n\xi_0. \tag{3.23}$$

At this level of approximation, the imaginary parts of c_0, and therefore the growth rates, are identical for the varicose and for the sinuous modes, and both cases differ only in the sign of the real phase velocity. Note that in this approximation the $n = 0$ varicose mode is neutral with trivial eigenfunctions, except in the strictly flat-sheet limit $\xi_0 \to \infty$.

3.2. *The structure of the eigenfunctions*

In the limit $n\xi_0 \to \infty$, all of the above eigenvalues become identical to those for the Kelvin–Helmholtz (K–H) instability of a flat vortex sheet, $c_0 = \pm\mathrm{i}$. For $n\xi_0 \gg 1$ and $n\xi \gg 1$ the corresponding eigenfunctions are proportional to

$$\widetilde{\phi}^{-}_{0,n} = \pm\mathrm{i}\,\mathrm{e}^{n(\xi-\xi_0)}, \quad \widetilde{\phi}^{+}_{0,n} = \mathrm{e}^{-n(\xi-\xi_0)}, \tag{3.24}$$

which also coincide with those of a flat sheet. This limit can occur in two ways which are in principle distinct, and which actually become so at higher orders of the α-expansion. If $\xi_0 \to \infty$ the sheet is flat, and the eigenmodes are pairs of oblique K–H waves with wave vectors $(\alpha, \pm n)$. If $n \gg 1$, even if the sheet is corrugated, the eigenfunctions have spanwise wavelengths which are short enough not to feel the curvature, and therefore behave as if the sheet were locally flat. The same is true in the limit of very short streamwise wavelengths, $\alpha \gg 1$, which also tends to K–H instability, and which is treated in Appendix A.

A few points should be mentioned. In the first place, the effect of the corrugation is always stabilizing, and the maximum growth rate, $\alpha\,\mathrm{Im}(c)$, is attained in the flat-sheet limit. This contradicts the experimental observation that streaks lift before bursting, and will be discussed in § 3.3. The effect is strongest for the low-order spanwise modes, and suggests that the initial breakdown of the streaks should be highly wrinkled, also contrary to observation. That conclusion is however most probably spurious, essentially similar to the property that the shortest waves are the most amplified in a flat sheet. That behaviour is linked to the zero thickness of the vorticity layer. If the velocity profile is made smooth, short waves are damped, and the most unstable wavelength is a low multiple of the layer thickness. That calculation is beyond the scope of this paper, but the same effect is likely to occur in the present case.

There is finally the question, posed in the introduction, of the 'family' to which the present instability belongs; whether to the 'wake family' proposed by Swearingen & Blackwelder (1987), or to the 'oblique K–H' one suggested by Schoppa & Hussain (1997). As with most taxonomical questions, the present results suggest that the truth is more a matter of terminology than of hard science. Our eigenvalues can be connected continuously with oblique K–H waves in the limit in which $\xi_0 \gg 1$, and with two-dimensional K–H waves in the opposite limit in which n and ξ_0 are kept constant and α is made large. For intermediate values of those parameters, even though the traces of a pair of oblique K–H waves can be seen in the eigenmodes for relatively small corrugations (see figure 3*a–d*), the eigenfunctions do not completely agree with any of those limits, and all that can be said is that they are variants of the K–H family.

Consider the spatial structure of the eigenfunctions. From (2.15) we obtain the perturbation to the location of the sheet as

$$\widetilde{\xi}_0 = -\mathrm{i}\frac{J|_{\xi=\xi_0}}{U - c_0}\left.\frac{\partial\widetilde{\phi}_0}{\partial\xi}\right|_{\xi=\xi_0}, \tag{3.25}$$

which, using the results of the previous section for the sinuous perturbation, leads to

$$\xi = \xi_0 + 2^{-1/2} n \mathrm{e}^{-n\xi_0} J|_{\xi=\xi_0} \sinh^{1/2} 2n\xi_0 \, \sin n\eta \, \mathrm{Re}\left\{C \, \mathrm{e}^{\mathrm{i}\alpha(x-ct)}\right\}. \tag{3.26}$$

The result for the varicose mode is similar, with $\cos n\eta$ substituted for the sine. The streamwise circulation density for the sinuous mode is obtained to leading order from (2.23) as

$$\Omega_x = 2n\alpha \mathrm{e}^{-n\xi_0} J^{1/2}\big|_{\xi=\xi_0} \sinh n\xi_0 \, \cos n\eta \, \mathrm{Re}\left\{C \, \mathrm{e}^{\mathrm{i}\alpha(x-ct)}\right\}, \tag{3.27}$$

and for the varicose one as

$$\Omega_x = -2n\alpha \mathrm{e}^{-n\xi_0} J^{1/2}\big|_{\xi=\xi_0} \cosh n\xi_0 \, \sin n\eta \, \mathrm{Re}\left\{C \, \mathrm{e}^{\mathrm{i}\alpha(x-ct)}\right\}. \tag{3.28}$$

Figure 3 shows the fundamental ($n = 1$) sinuous and varicose eigenstructures for $\xi_0 = \frac{1}{2}\pi$, $\frac{1}{3}\pi$ and $\frac{1}{6}\pi$. The figure includes the perturbed vortex sheet, its streamwise circulation density, and the disturbance velocities in a cross-plane. For the less corrugated sheet in figures 3(*a*) and 3(*b*), the positive and negative streamwise vorticities are arranged in a checkerboard pattern which is strongly reminiscent of a pair of oblique K–H instability waves. As ξ_0 is made smaller, and the sheet becomes more corrugated in figure 3(*c–f*), the disturbance vorticity becomes localized near the crest of the sheet, and the pattern differs from that of oblique K–H waves. This behaviour stems from the properties of the Jacobian. As ξ_0 decreases and the corrugation becomes sharper, the Jacobian (2.11) becomes larger near the crests, and it follows from (3.26)–(3.28) that both the sheet deformation and the streamwise vorticity tend to concentrate where J is largest.

It is interesting to compare the magnitude of (3.27) and (3.28) with the other components of the perturbation vorticity. Consider for example the spanwise component Ω_z which is of order $l_y\alpha^2[\phi_0]$, where l_y is the vertical component of the unit vector normal to the sheet, and is always $O(1)$. The magnitude of (3.27) is $\Omega_x \approx J^{1/2} n\alpha[\phi_0]$, so that their ratio is $\Omega_x/\Omega_z \approx nJ^{1/2}/(\alpha l_y)$. When the corrugation of the sheet is small this ratio is $O(n/\alpha)$, as it would be for classical oblique waves but, as the corrugation increases and J becomes locally large, the streamwise vorticity becomes the dominant component.

Although our simplified model is too different from the fairly low-Reynolds-number streaks of real wall layers to allow useful quantitative comparisons, some qualitative remarks can be made. If we assume that the near-wall streaks have a spanwise spacing of 100 wall units, and a height of around 40, which is typical of the buffer layer, their aspect ratio would be around 0.4. This is in between the cases in figures 3(*c*) and 3(*e*), and the eigenfunction in figure 3(*c*) is indeed remarkably similar to those found for model streaks by Waleffe & Kim (1997) and Schoppa & Hussain (1997). The alternation of streamwise vortices of opposite signs along the crest induces in the streak a sinuous deformation which is also reminiscent of observations at an initial stage of the streak instability. Further comparisons with known nonlinear solutions of the Navier–Stokes equations will be made in § 5.

3.3. *The influence of the wall*

We have noted above that the result that the corrugation of the vortex sheet is stabilizing is difficult to reconcile with the experimental evidence. It has been clear since the initial observations of Kim, Kline & Reynolds (1971) that the instability of the streaks is enhanced when they are lifted away from the wall, and it is at that moment that the corrugation of the vorticity layer is largest. The problem with our

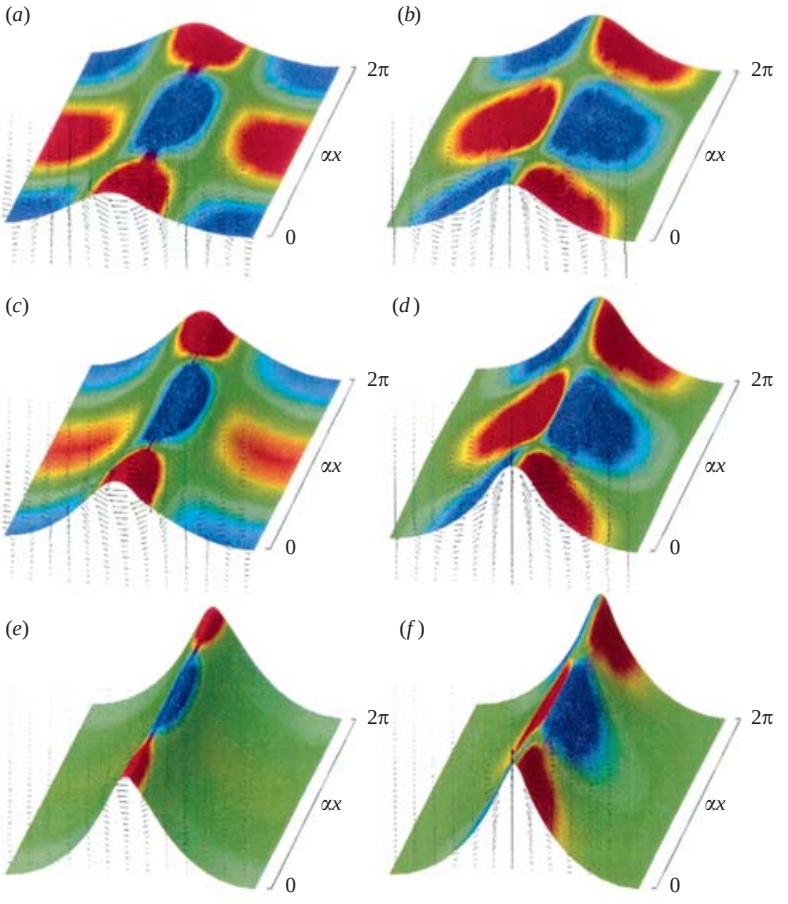

FIGURE 3. For caption see facing page.

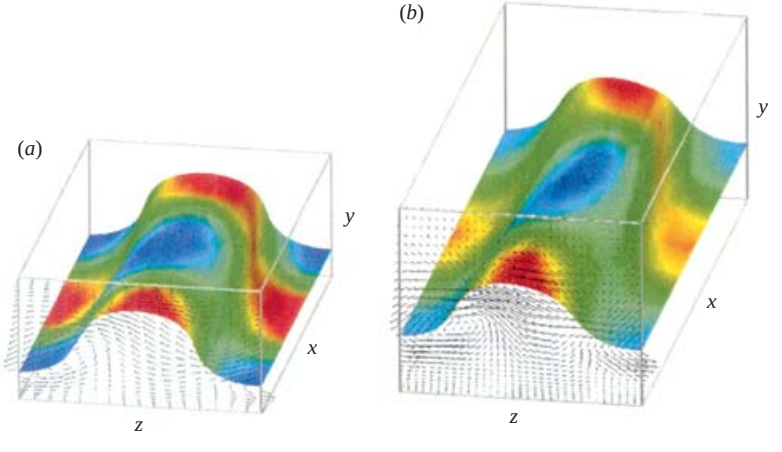

FIGURE 10. For caption see facing page.

previous analysis is that, although the corrugation of the vorticity layer representing the streak was incorporated into (2.9), the wall was not.

The presence of a nearby wall inhibits instability. In the inviscid approximation used in this paper, the instability of a flat vortex sheet, lying initially at a distance H from a wall, is equivalent to the varicose mode of a plane jet with the top-hat velocity profile

$$U = 1 \quad \text{when} \quad |y| > H, \qquad U = -1 \quad \text{otherwise.} \tag{3.29}$$

Its eigenvalues were shown by Rayleigh (1879) to be

$$c = -\exp(-2\overline{\alpha}H) \pm \mathrm{i}(1 - \exp(-4\overline{\alpha}H))^{1/2}, \tag{3.30}$$

where $\overline{\alpha}^2 = \alpha^2 + \beta^2$, and β is the spanwise wavenumber. The imaginary part of (3.30) asymptotes to $c_i = \pm 1$ when $\overline{\alpha}H \gg 1$, as in the classical K–H case, but decreases rapidly when $\overline{\alpha}H \lesssim 1$, and vanishes when the sheet coincides with the wall. When a streak is lifted, it is therefore subject to two opposing effects. Moving away from the wall makes it more unstable, while the warping stabilizes it. To explore the interaction between these two effects we introduce a new conformal map,

$$\chi = \log \sin\left(\frac{\mathrm{i}a + \zeta}{2}\right) - \log \sin\left(\frac{\mathrm{i}a - \zeta}{2}\right), \tag{3.31}$$

where $a \geqslant 0$. This map is anti-symmetric with respect to $\zeta = 0$, and periodic in η and z with period 2π (figure 4*a*), with a branch cut connecting through infinity the two singularities $\zeta = \pm \mathrm{i}a$. Only isolines $\xi = \xi_0$ for which $-a < \xi_0 < a$ define singly connected vortex sheets, in which case the isoline $\xi = -\xi_0$ defines another sheet which is the reflection of the first one with respect to $y = 0$. The limits $y \to \pm\infty$ map into $\zeta = 2k\pi \pm \mathrm{i}a$, and the z-axis maps into $\xi = 0$. Flat sheets are obtained in the limit of constant ξ_0 and $a \to \infty$ (figure 4*b*).

We can therefore construct flow fields which are consistent with an inviscid wall along the z-axis by using velocity potentials which are symmetric in ξ. We shall assume that the velocity jump is defined as in (3.29),

$$U = 1 \quad \text{when} \quad |\xi| > \xi_0, \qquad U = -1 \quad \text{otherwise.} \tag{3.32}$$

FIGURE 3. Unstable fundamental eigenstructures of a corrugated vortex sheet for $n = 1$. The streamwise circulation density in the perturbed vortex sheet is shown for: (*a*, *b*) $\xi_0 = \frac{1}{2}\pi$, (*c*, *d*) $\frac{1}{3}\pi$, and (*e*, *f*) $\frac{1}{6}\pi$. Red is positive and blue is negative. See figure 2 for the unperturbed shapes of the vortex sheets. (*a*, *c*, *e*) Sinuous modes. (*b*, *d*, *f*) Varicose modes. The disturbance velocity vectors, in a frame of reference moving with the real part of the phase velocity, are shown in the plane $x = 0$. One wavelength is shown both in the x- and in the z-direction.

FIGURE 10. Three-dimensional nonlinear equilibrium solutions for wall-bounded shear flows. (*a*) Nagata's (1990) (lower-branch) stationary solution to a plane Couette system. (*b*) Toh & Itano's (1999, 2001) travelling wave solution to a plane Poiseuille system. The upper (lower) wall moves into (out of) the page in (*a*), while the flow is into the page in (*b*). The streamwise vorticity is shown on the critical layer. Red is positive and blue is negative. The cross-flow velocity vectors are also shown on the plane $x = 0$. One periodic box is shown in the x- and the z-direction. In (*a*) the Reynolds number, based on channel half-width, h, and on half the difference of the two wall velocities, is 400, and the streamwise and the spanwise periods are $2\pi h$ and $1.2\pi h$, respectively. In (*b*), the Reynolds number, based on h and on the mean bulk velocity, is 2000, and the streamwise and the spanwise periods are πh and $0.4\pi h$, respectively. Only half the height of the channel is shown in (*b*).

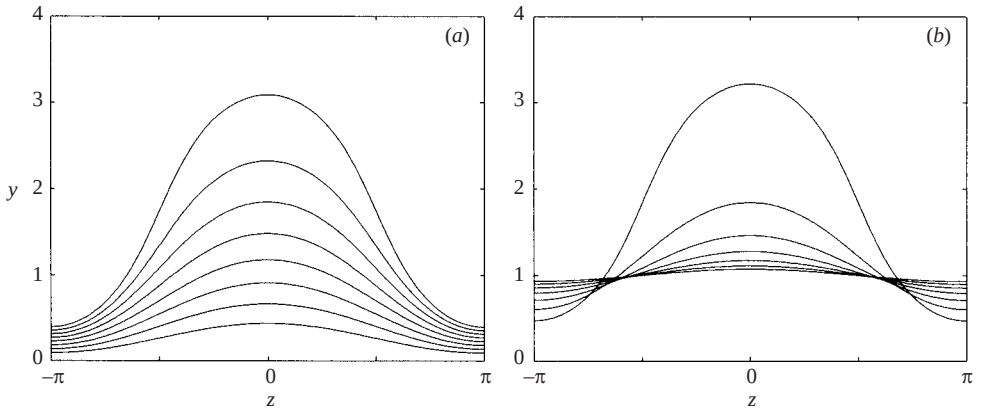

FIGURE 4. ξ-isolines of the map (3.31). In all the cases the isoline $-\xi$ is the reflection with respect to $y = 0$ of the lines shown here. (*a*) $a = 1$, and $\xi_0/a = 0.2(0.1)0.9$, increasing upwards. (*b*) $\xi_0 = 1$, and $a/\xi_0 = 1.1(0.4)3.5$, in order of increasing flatness.

By arguments similar to those in the previous subsection, the sinuous perturbation mode has, to lowest order in α, the form

$$\widetilde{\phi}_0^{\pm} = \widetilde{\phi}_{0,n}^{\pm}(\xi)\sin n\eta, \tag{3.33}$$

where n is any integer greater than zero, and the impermeability at the wall requires that

$$\left.\frac{\mathrm{d}\widetilde{\phi}_{0,n}^{-}}{\mathrm{d}\xi}\right|_{\xi=0} = 0. \tag{3.34}$$

Above the sheet, the derivative

$$\frac{\mathrm{d}\zeta}{\mathrm{d}\chi} = -\mathrm{i}\frac{\cosh a - \cos\zeta}{\sinh a} \tag{3.35}$$

only attains infinity in the limits $\xi \to \pm\infty$, which map into $\chi = \pm a + (2k+1)\pi\mathrm{i}$. Since the velocity should remain regular at those points, an argument similar to the one leading to (3.14) requires that the potential should vanish in that limit, so that

$$\widetilde{\phi}_{0,n}^{-} = \cosh n\xi, \qquad \widetilde{\phi}_{0,n}^{+} = B\mathrm{e}^{-n\xi}. \tag{3.36}$$

The jump conditions (3.5) and (3.6) result in

$$c_0 = -\mathrm{e}^{-2n\xi_0} \pm \mathrm{i}\left(1 - \mathrm{e}^{-4n\xi_0}\right)^{1/2}, \tag{3.37}$$

which is identical to (3.22). In this case the conditions to be satisfied by the varicose and sinuous modes are identical, and so are the eigenvalues.

The flat vortex sheet at a distance H from the wall is obtained from (3.31) by letting $\xi_0 = H$, and $a \to \infty$. In this limit we have $\overline{\alpha} = n$, to lowest order in α, and we recover (3.30) for both the varicose and the sinuous mode.

Note that, although the magnitude of the eigenvalue does not depend on the parameter a, the shape of the vortex sheet does, so that (3.31) can be used to differentiate between the effects of the wall distance and of the warping on the instability. The imaginary part of (3.37) is plotted in figure 5(*a*) as a function of the minimum and maximum heights of the sheet above the wall. It is clear from that figure that the damping is predominantly controlled by the minimum wall distance, y_{min}, and it is easy

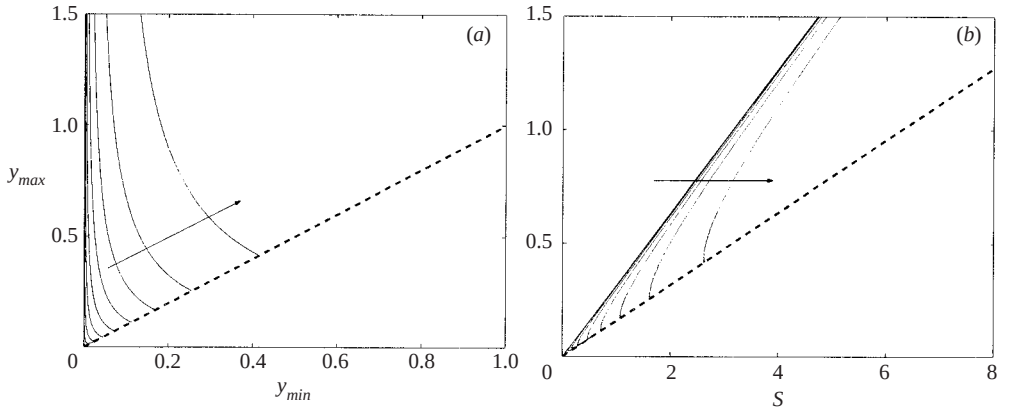

FIGURE 5. Imaginary part of the instability eigenvalue (3.37), for the vortex sheets defined by (3.31). $n = 1$. (*a*) As a function of the maximum and minimum height of the sheet. (*b*) As a function of the maximum height and the area underneath the sheet. The contours are $\mathrm{Im}(c_0) = 0.1(0.1)0.9$, increasing in the direction of the arrows. The dashed line is in both cases the locus of flat sheets for which $y_{max} = y_{min}$.

to show that the sheet is neutrally stable as long as $y_{min} = 0$. Lifting the crest of the streak overcomes this effect, and the streak becomes more unstable as the maximum streak height, y_{max}, increases. In their viscous smooth model for streaks Schoppa (2000) and Schoppa & Hussain (2002) observed that lifted streaks are more unstable.

A somewhat different view of the same data is figure 5(*b*), where the imaginary part of the eigenvalue is plotted as a function of y_{max} and of the area S underneath the vortex sheet. During the inviscid lifting of a sheet away from the wall the latter is conserved, since no fluid can cross the vortex surface, and the point representing the streak in this plot traverses an ascending vertical trajectory. It is interesting that the effect of such a lifting process is to inhibit the instability, essentially because the only way to lift the crest of a streak is to lower its valley towards the wall. The lower line bounding the region of possible (S, y_{max}) combinations is $S = 2\pi y_{max}$, and corresponds to the area underneath flat sheets. The upper one is $S = \pi y_{max}$, which corresponds to the family of sheets that touch the wall, $a = 0$. The instability growth rate vanishes for all the sheets in this family. The consequences of this observation will be briefly explored in § 5.

It follows from (2.23) and (3.33) that the amplitude of the streamwise vorticity perturbation of the sinuous mode is proportional to

$$\Omega_x \sim J^{1/2} \cos n\eta = \frac{|\cosh a - \cos\zeta|}{\sinh a} \cos n\eta, \tag{3.38}$$

while that of the varicose mode is proportional to

$$\Omega_x \sim J^{1/2} \sin n\eta. \tag{3.39}$$

Thus, as in the case of the free vortex sheet, the streamwise vorticity of the sinuous mode tends to concentrate at the peaks and at the valleys of the sheet, while that of varicose mode tends to be located at the inflection points. The effect of the Jacobian, and of the geometric deformation due to the mapping, can however be substantial, and tends to shift the vortices to the locations where the mapping is more singular. In the free sheets of the previous subsection those were the sharp peaks of the lifted streaks, but here they are the valleys where the sheet approaches the wall.

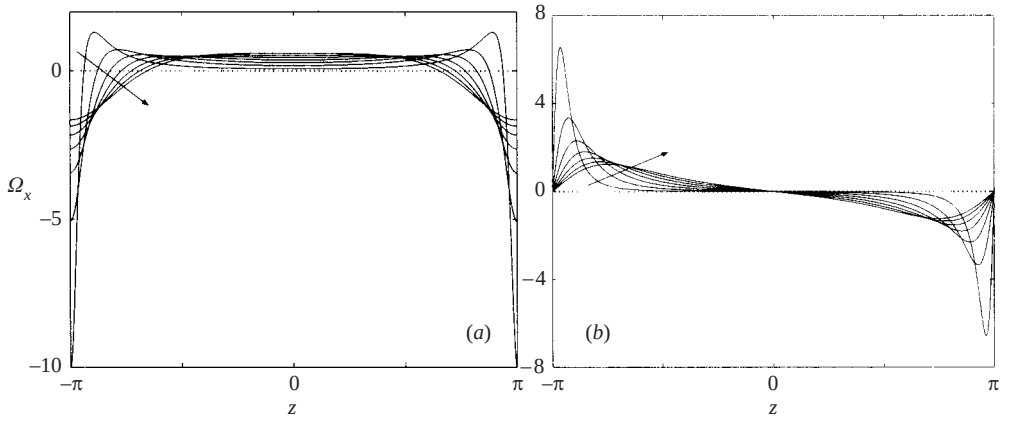

FIGURE 6. Streamwise vorticity distribution along the vortex sheet for the $n = 1$ eigenfunctions, as a function of the spanwise coordinate z. In all cases $\xi_0 = 0.1$ and the parameter $a = 0.2(0.2)1.4$ increases in the direction of the arrows. The vorticity is in arbitrary units, but the maximum of the jump $[\phi]$ of the perturbation potential is kept constant among cases. (*a*) Sinuous mode. (*b*) Varicose mode.

The spanwise distribution of streamwise vorticity in the eigenfunctions is shown in figure 6 for a family of vortex sheets with a fixed value of ξ_0 but with different values of a. Specially in the cases in which a is small, and the valley of the sheet comes very close to the wall, the vortices of the sinuous mode are located there, with much weaker countervortices near the top of the layer. The vortices of the symmetric 'hairpins' of the varicose perturbations are also in this case close to the valleys. Although the vorticity magnitude used in the figure is arbitrary, the potential jump $[\widetilde{\phi}_0]$ has been kept constant among the different traces, so that the values in the figure are roughly proportional to the ratio, $\alpha\Omega_x/\Omega_z$, between the streamwise and spanwise perturbation vorticities. Note that the stability characteristic of all the sheets used for figure 6 are identical, in spite of the large differences among their streamwise vorticity distributions.

We have already noted that it is difficult to make quantitative comparisons with experimental streaks, since the velocity profile used here is very different from the real ones, but some qualitative conclusions can be drawn. One of the salient features of the sinuous streaks observed in experiments and simulations is the presence of a single staggered vortex pair per longitudinal wavelength, which agrees with the dominance of either the valley or the peak vortices in the instability eigenfunctions. The location of the observed experimental vortices is also consistent with the valleys, since they are generally reported to lie in the high-speed part of the streak, rather than above its low-speed region, again as in figure 6. Also, the average height of the centre of the vortices above the wall is $y^+ \approx 20$, while the streak itself is at least twice as high (Kim, Moin & Moser 1987).

4. Higher-order corrections

We next outline the procedure to obtain the second-order corrections to the eigenvalues of the free vortex sheet. For the sinuous mode, it follows from (2.12) and (3.10) that the inhomogeneous term in the second-order equation (3.7) has the

Fourier expansion

$$J^{-1}\widetilde{\phi}_0^{\pm} = \sum_{m=1}^{\infty} g_m^{\pm} \sin m\eta, \tag{4.1}$$

where

$$g_m^{\pm}(\xi) = \begin{cases} \frac{1}{2}(2j_0 - j_{2n})\widetilde{\phi}_{0,n}^{\pm} & (m = n) \\ \frac{1}{2}(j_{|m-n|} - j_{m+n})\widetilde{\phi}_{0,n}^{\pm} & (m \neq n), \end{cases} \tag{4.2}$$

so that the solution to (3.7) can be written as

$$\widetilde{\phi}_2^{\pm} = \sum_{m=1}^{\infty} \widetilde{\phi}_{2,m}^{\pm}(\xi) \sin m\eta. \tag{4.3}$$

Note that the summation convention is not used for repeated subscripts in this paper. For the varicose mode, the Fourier expansion of the inhomogeneous term in (3.7) is

$$J^{-1}\widetilde{\phi}_0^{\pm} = \sum_{m=0}^{\infty} g_m^{\pm} \cos m\eta, \tag{4.4}$$

where

$$g_m^{\pm}(\xi) = \begin{cases} \frac{1}{2} j_n \widetilde{\phi}_{0,n}^{\pm} + j_0 G^{\pm} & (m = 0) \\ \frac{1}{2}(2j_0 + j_{2n})\widetilde{\phi}_{0,n}^{\pm} + j_n G^{\pm} & (m > 0 \text{ and } m = n) \\ \frac{1}{2}(j_{|m-n|} + j_{m+n})\widetilde{\phi}_{0,n}^{\pm} + j_m G^{\pm} & (m > 0 \text{ and } m \neq n), \end{cases} \tag{4.5}$$

with

$$G^- = -(-1)^n \widetilde{\phi}_{0,n}^-(0), \quad G^+ = (-1)^n \frac{1 + c_0}{1 - c_0} \widetilde{\phi}_{0,n}^-(0), \tag{4.6}$$

and the solution to (3.7) has the form

$$\widetilde{\phi}_2^{\pm} = \sum_{m=0}^{\infty} \widetilde{\phi}_{2,m}^{\pm}(\xi) \cos m\eta. \tag{4.7}$$

Substitution of (3.10) and (4.3), or of (3.21) and (4.7), into (3.7)–(3.9) yields

$$\left(\frac{\mathrm{d}^2}{\mathrm{d}\xi^2} - m^2\right) \widetilde{\phi}_{2,m}^{\pm} = g_m^{\pm}, \tag{4.8}$$

$$(1 - c_0)\widetilde{\phi}_{2,m}^{+} + (1 + c_0)\widetilde{\phi}_{2,m}^{-} = c_2\, \delta_{mn}[\widetilde{\phi}_{0,n}] \quad \text{on } \xi = \xi_0, \tag{4.9}$$

$$(1 + c_0)\frac{\mathrm{d}\widetilde{\phi}_{2,m}^{+}}{\mathrm{d}\xi} + (1 - c_0)\frac{\mathrm{d}\widetilde{\phi}_{2,m}^{-}}{\mathrm{d}\xi} = -c_2\, \delta_{mn}\left[\frac{\mathrm{d}\widetilde{\phi}_{0,n}}{\mathrm{d}\xi}\right] \quad \text{on } \xi = \xi_0, \tag{4.10}$$

where δ_{mn} is the Kronecker delta. The solvability condition for this inhomogeneous system determines the second-order correction c_2 to the eigenvalue.

The corresponding homogeneous problem is the same as the one solved for the leading-order approximation in § 3.1, and its solution is either the sinuous pair (3.19)–(3.20), or the varicose one (3.22)–(3.23), with n replaced by m. Since the modal two-dimensional Laplacian operator in (4.8) is self-adjoint, Green's formula yields

$$\left[\widetilde{\phi}_{2,m}\frac{\mathrm{d}\widetilde{\phi}_{0,m}}{\mathrm{d}\xi} - \frac{\mathrm{d}\widetilde{\phi}_{2,m}}{\mathrm{d}\xi}\widetilde{\phi}_{0,m}\right] = \int_0^{\infty} g_m \widetilde{\phi}_{0,m}\, \mathrm{d}\xi. \tag{4.11}$$

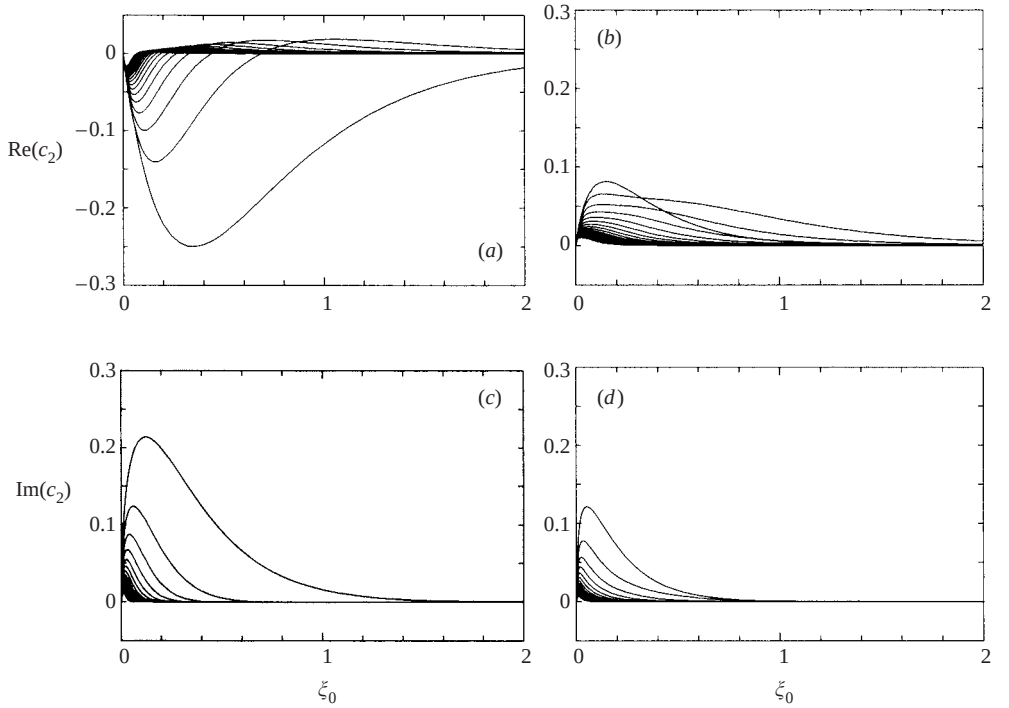

FIGURE 7. Variation of the second-order correction c_2 to the unstable eigenvalue, against the corrugation parameter ξ_0 for orders $n = 1$–20, in the wall-free case. (*a*,*c*) Sinuous mode. (*b*,*d*) Varicose mode. (*a*,*b*) Real part of c_2. (*c*,*d*) Imaginary part of c_2. In all cases higher orders correspond to weaker corrections.

Substituting (4.9) and (4.10) in the left-hand side of this equation, c_2 only appears when $m = n$, and the solvability condition is

$$c_2 = \frac{\displaystyle\int_0^\infty g_n \widetilde{\phi}_{0,n}\,\mathrm{d}\xi}{\dfrac{4}{1-c_0^2}\widetilde{\phi}^+_{0,n}\left.\dfrac{\mathrm{d}\widetilde{\phi}^+_{0,n}}{\mathrm{d}\xi}\right|_{\xi=\xi_0}}. \tag{4.12}$$

The detailed expressions for c_2 in the sinuous and in the varicose modes are cumbersome, and are given in Appendix B, but we should note that, in contrast to the leading-order eigenvalue, the second-order correction involves n and ξ_0 independently rather than as the combination $n\xi_0$. Equation (4.11) with $m \neq n$ gives the magnitude of those harmonics in the second-order corrections to the eigenfunctions. Figure 7 shows the real and imaginary parts of c_2 against ξ_0 for the sinuous and for the varicose modes. It can be seen that c_2 tends to zero both for $\xi_0 \gg 1$ and for $n \gg 1$. At the leading order those two limits were connected with the K–H instability of a flat vortex sheet, and in that case the lowest-order approximation already gives the exact expression for the eigenvalues.

The trends of the second-order correction to the imaginary part of the eigenvalue are opposite to those of the lowest-order solution. While the latter became more stable with decreasing ξ_0 and decreasing n, the correction behaves the other way around, at least for $\xi_0 \gtrsim 0.2$. This suggest that for the free vortex sheet there could be an intermediate ξ_0 for which the total eigenvalue $c_0 + \alpha^2 c_2$ would be most unstable.

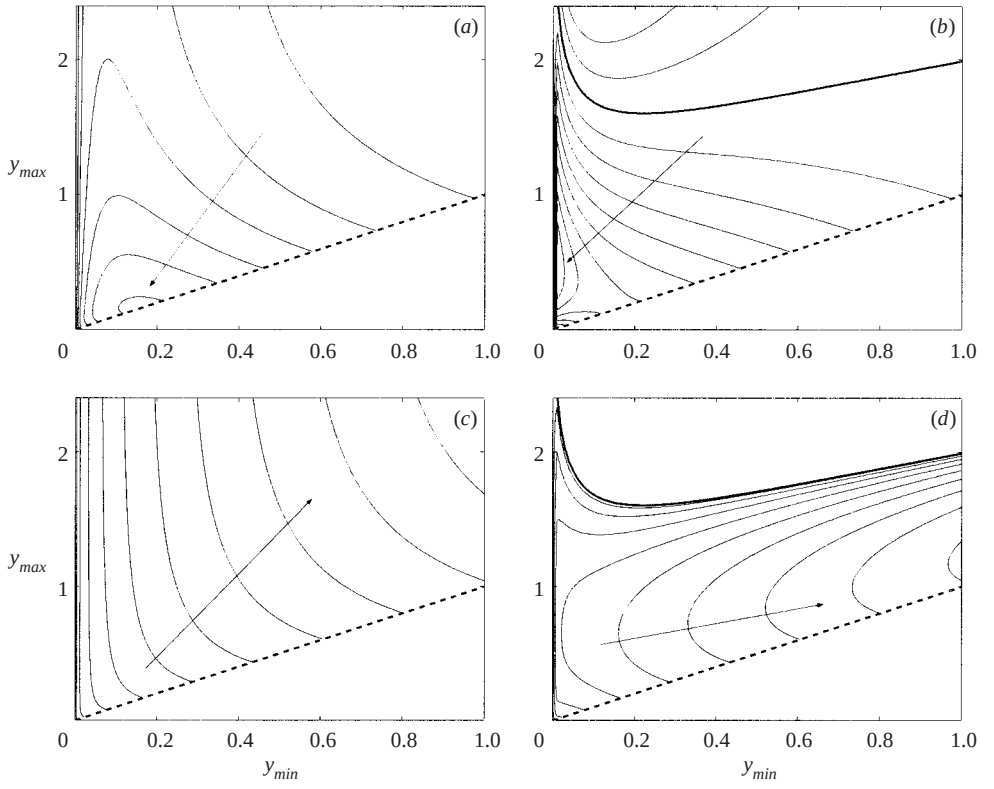

FIGURE 8. Variation of the second-order correction to the imaginary part of the unstable eigenvalue in the wall-bounded case, as a function of the minimum and maximum wall-distance of the corrugated sheet. (*a*) Sinuous case. Isolines are $\mathrm{Im}(c_2) = 0.02(0.02)0.12$. (*b*) Varicose mode. Isolines are $\mathrm{Im}(c_2) = -0.04(0.02)0.16$. Isolines above the heavier line are negative. (*c*,*d*) Same data expressed as wavelengths, as defined in (4.13). (*c*) Sinuous mode. Isolines are $\lambda_0 = 1(1)10$. (*d*) Varicose mode for positive $\mathrm{Im}(c_2)$. Isolines are $\lambda_0 = [0(1)9]$. In all cases the isolines increase in the direction of the arrows.

That turns out not to be the case. For $\alpha \lesssim 1$, where the asymptotic expansion might be expected to be of some value, the most unstable case is always the flat layer.

It is interesting to note, on the other hand, that the corrections to the varicose case are more stable than those to the sinuous one (see figures 7*c* and 7*d*), in agreement with those obtained by Kawahara *et al.* (1998) for smooth viscous streaks.

In the wall-bounded case the corrections are computed in a similar way, although the Fourier coefficients of the Jacobian can only be easily expressed analytically for the lowest spanwise modes. They are given at the end of Appendix B for $n = 1$, and the corresponding stability corrections are plotted in figures 8(*a*) and 8(*b*). As in the free vortex sheet, the sinuous mode is more unstable than the varicose one for finite wavelengths. The only exception is when y_{min} is very small, but we have already seen that this limit is in any case strongly stabilized by the wall and unlikely to lead to breakdown.

Note that, at least when $\mathrm{Im}(c_2) > 0$, the first two terms of the eigenvalue expansion define a scale,

$$\lambda_0 = 2\pi \left[\frac{\mathrm{Im}(c_2)}{1 - \mathrm{Im}(c_0)} \right]^{1/2}, \tag{4.13}$$

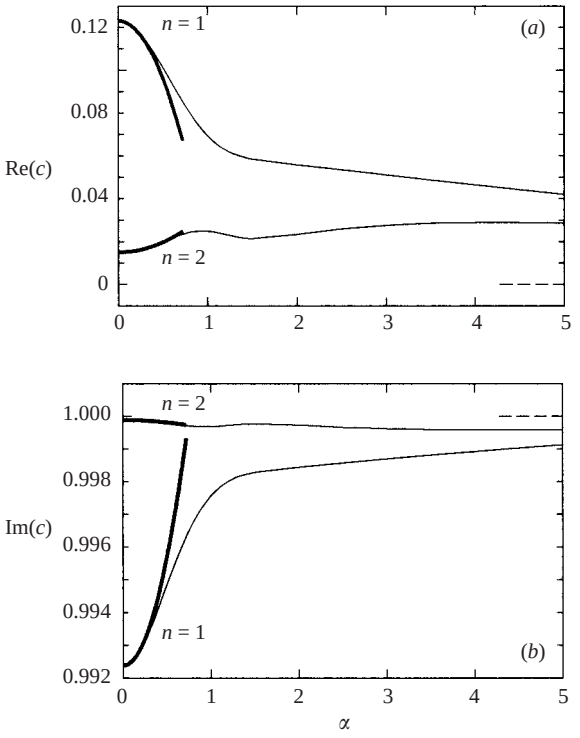

FIGURE 9. Variation of the unstable eigenvalues of the first two sinuous modes of a free corrugated vortex sheet with $\xi_0 = \frac{1}{3}\pi$, against the streamwise wavenumber. (*a*) Real part of c. (*b*) Imaginary part of c. The thick curves represent the long-wave asymptotic approximations to the eigenvalues, $c = c_0 + \alpha^2 c_2$. The thin curves denote the two numerical eigenvalues continued from the leading-order approximations c_0 at $\alpha \to 0$. The dashed horizontal lines represent the short-wavelength asymptotics $c = +\mathrm{i}$ at $\alpha \gg 1$.

for the wavelength at which the growth rate achieves its asymptotic short-wavelength value $\mathrm{Im}(c) = 1$. This length scale has been plotted in figure 8(*c*) for the sinuous mode in the wall-bounded case and, as in the case of the lowest-order expansion, it is seen that the main influence is the minimum distance from the sheet to the wall. Note also that the wavelengths implied are short, except for very lifted layers in which the growth rate is in any case similar to a free flat sheet, giving some hope that the asymptotic series can be trusted over a relatively wide range of wavenumbers. The results for the varicose mode are include in figure 8(*d*), for comparison.

4.1. *Numerical results*

Both to study the behaviour at intermediate wavenumbers, and to check the accuracy of the various asymptotic expansions, the eigenvalues of the sinuous modes of the free vortex sheet were computed numerically for a range of wavenumbers, and for various corrugation amplitudes. The numerical code uses fourth-order finite differences in ξ and a Fourier sine expansion in η, and is briefly described in Appendix C.

Figure 9 shows the dependence on the wavenumber of the first two unstable eigenvalues in the case $\xi_0 = \frac{1}{3}\pi$. Recall that this was the sheet which was judged in figure 3(*c*) to be geometrically closest to the experimental streaks. In the figure,

the thick curves represent the long-wavelength asymptotics, $c = c_0 + \alpha^2 c_2$, the thin curves represent the numerically computed eigenvalues, and the dashed horizontal lines denote the short-wavelength behaviour, $c = \mathrm{i}$. It can be seen that the long-wave approximation is in excellent agreement with the numerical values up to relatively large streamwise wavenumbers.

It can also be seen from the scale in figure 9(*b*) that, even for these relatively strong corrugations, the effect of the curvature is relatively small, and that the growth rate is fairly close to its K–H value at all wavenumbers. This is even more apparent for the higher spanwise orders, of which only $n = 2$ is shown in the figure.

The analysis presented in this section can be carried out in the same way for the wall-bounded case in § 3.3, but it is unlikely to provide new information. Part of the interest of the present section is to ascertain that the asymptotic series can be consistently extended to higher orders, which is a well-known pitfall in this sort of analysis. Once this has been checked for the free vortex layer, and since the the expansion procedure is the same in both cases, there is no reason to doubt that it would also be true for the wall-bounded one.

5. Discussion and conclusions

We have analysed the unstable eigensolutions of a corrugated vortex sheet, and shown that they in general contain streamwise vorticity, which becomes dominant both when the corrugation is large and when the sheet approaches a wall. Such instabilities are therefore good candidates for the generation mechanism of streamwise vortices in the near-wall layer of turbulent flows. We mentioned in the introduction the numerical and experimental evidence for their occurrence in natural and model flows. We shall now centre on the similarities and differences between the computed eigenfunctions and fully nonlinear solutions, to inquire to what extent the nonlinear structures can be considered saturated stages of the instabilities studied here.

Schoppa & Hussain (1997, 1998) followed numerically the evolution of the unstable streaks in minimal plane Poiseuille flow to obtain transient structures which were quite similar to those observed in near-wall turbulence. More recently, Toh & Itano (1999, 2001) investigated the nonlinear saturation of the instability of a particular class of streaks in minimal Poiseuille flow, and observed that a system approaches a three-dimensional nonlinear permanent travelling-wave solution, i.e. a fixed point in phase space, whose spatial structure is very similar to that in Schoppa & Hussain (1997, 1998). Equivalent fixed points, although with a different symmetry with respect to the channel centreline, had been obtained exactly in Poiseuille flows using the Newton method by Waleffe (1998, 2001), who noted the similarity between near-wall coherent structures and the spatial structure of the fixed points. The translation velocity of Toh & Itano's (1999, 2001) travelling wave is very close to the volume-averaged bulk velocity of the flow in the channel. Itano & Toh (2001) interpreted the instability of their streaks as the approach of the system to the unstable fixed point along its stable manifold. The bursting process would then be the succeeding escape along the unstable manifold, possibly related to subcritical transition through streak breakdown (Reddy *et al.* 1998). Fixed points of the same type have been obtained using different techniques by Jiménez & Simens (2001). Kawahara & Kida (2001) later identified Toh & Itano's (1999, 2001) wave as the same kind of fixed point as Nagata's (1990) older three-dimensional nonlinear (lower-branch) stationary solution for plane Couette flow. Since the former was found as the nonlinearly saturated state of a streak instability,

it is interesting to compare both solutions with our analytical eigensolution for the corrugated vortex sheet.

Figures 10(*a*) and 10(*b*) (see p. 326) show respectively Nagata's (1990) and Toh & Itano's (1999, 2001) permanent waves. They are printed next to figure 3 to facilitate comparison. Both solutions have been recomputed for the purpose of this paper using a shooting method similar to the one in Toh & Itano (1999, 2001). Because the streamwise vorticity is observed in smooth streak models to be concentrated around the critical layer (Schoppa & Hussain 1997; Kawahara *et al.* 1998; Itano & Toh 2001), we have drawn in the figure only the surface where the streamwise velocity component $u(x, y, z)$ is equal to the translation velocity of the equilibrium waves. To make the representation comparable with the eigenfunctions in figure 3, the streamwise vorticity is drawn on that surface, and the perturbation cross-flow velocities are shown at $x = 0$. It is clear from the figure that the two nonlinear equilibrium solutions are qualitatively very similar. Waleffe (1998) also reported a close similarity between (upper-branch) three-dimensional nonlinear equilibrium solutions for plane Couette and Poiseuille flows under fixed-stress wall-boundary conditions. The spatial structures in figure 10 are characterized by streamwise vortices of alternating sign in a staggered longitudinal array along the low-speed streak, and they broadly resemble the coherent structures observed in near-wall turbulence (Stretch 1990; Jeong *et al.* 1997). The most obvious difference between the Couette and Poiseuille equilibrium solutions is that, while the former is symmetric between crests and valleys, the latter is not, which is an obvious consequence of the different symmetries of the two problems. Differences between minimal turbulent Couette and Poiseuille flows were reported in Schoppa & Hussain (1998). It is also apparent from comparing figure 10 with figure 3(*c*) that the nonlinear solutions are related to the unstable sinuous eigenfunctions, in agreement with the experiments quoted above for smooth velocity models. The main difference between the linear and the nonlinear solutions is the presence in the latter of somewhat stronger vortices near the valleys, particularly visible in the velocity field in figure 10(*b*). This is also true of experimental streaks, and was attributed by Schoppa & Hussain (1997) to vortex stretching due to the bending of the streak. Our discussion in § 3.3, in which vortex stretching is absent, while the intensification of the valley vortices is traced to the geometric factor coming from the Jacobian, gives strong support to the alternative model that the strengthening is due to the constraining effect of the nearby wall on the transverse velocities.

An interesting question is whether the nonlinear phase of the corrugated sheet instability discussed in this paper would lead to an analytical interpretation of the above nonlinearly saturated states, but this requires a completely different approach from the one used here, and is left for future studies.

In summary, we have presented in this work analytical eigensolutions for the inviscid instability of a corrugated vortex sheet. We have shown that the transverse curvature is always stabilizing in the case of free sheets. The effect is more complicated in the vicinity of a wall, because the presence of the wall itself is stabilizing, and the warping of the layer is accompanied by lifting of part of the sheet away from the wall. In any case, the instability of these warped sheets is always weaker than the classical Kelvin–Helmholtz instability of plane free vortex layers. In both the free and the wall-bounded cases we have linked the instabilities to oblique Kelvin–Helmholtz waves in appropriate related flows, and we have shown that the local intensification of streamwise vorticity can be traced to the geometric properties of the sheet. In general we find that the stability characteristics of our wall-bounded models sheets are primarily controlled by their minimum distance to the wall.

The sinuous mode is, in all cases of interest, more unstable than the varicose one, although it is interesting that the difference only appears in the higher-order wavenumber corrections. This behaviour is reminiscent of that of a vortex sheet of elliptical cross-section, which was analysed by Crighton (1973). A periodic array of such sheets could perhaps be considered as a very rough model for an extremely corrugated vortex layer, and can actually be constructed from isolines of the mapping (3.31) with $|\xi| > a$. The instability modes of such jets are also oblique, and their growth rates are also identical for the sinuous and varicose symmetries in the limit of very long wavelengths. The finite-wavelength behaviour found here is in agreement with that of smooth streak models, in which the sinuous mode is consistently more unstable than the varicose one (Schoppa & Hussain 1997; Kawahara *et al.* 1998).

An interesting aspect of the present simplified model is the conclusion from figure 5(*b*) that the inviscid lifting of a streak stabilizes it by forcing parts of the shear layer against the wall, although the streak becomes more unstable when its maximum height is increased for the *fixed* minimum wall distance. This is contrary to observations in turbulent flows, and is linked to the conservation of the volume underneath the sheet. It can be bypassed either by considering three-dimensional lifting, which allows axial drawing of fluid along the streak, or by viscous diffusion. The first process begs the question of how the three-dimensionality is generated in the absence of an instability, but the second one is interesting because it naturally introduces a critical Reynolds number, and therefore a critical streak size. The predominant size of the streaks, and in particular the commonly agreed value of 100 wall units, is clearly a Reynolds number, but it is intuitively a little too high to be taken as a threshold for an inviscid instability such as Kelvin–Helmoltz. It would make more sense if it could be considered as a measure of the dimensionless distance from the wall at the lowest point of the streak. In essence, what the present results suggest is that advective lifting by itself is not enough to destabilize a streak, and that the corrugation of the wall layer grows until viscous diffusion has separated it enough from the wall. Any quantitative estimate of the resulting threshold is of course beyond the present inviscid model.

We have noted that, despite the drastic simplification of the smooth velocity distribution by a sharp velocity jump, the structure of the eigenfunctions remarkably similar both to the numerically computed eigenfunctions of smooth flow models, and to the nonlinear flow structures observed in full simulations of near-wall streaks. It is therefore likely that the essential instability mechanism of the more realistic flows are captured by our simpler model, which could therefore be used to explore in detail its properties, eventually perhaps leading to the formulation of more efficient control strategies. The above discussion of the qualitative effects of the different geometrical parameters of the warped sheets is an example of such an exploration, which would have taken considerably more work if it had been undertaken using more general models.

This work was started while G. K. was visiting the Universidad Politécnica de Madrid (UPM) and the Centre for Turbulence Research (CTR). The kind hospitality of all at UPM and CTR is gratefully acknowledged. G. K. appreciates helpful discussions with Professors S. Yanase, K. Amano and H. Ito in the development of this study. This work was partially supported by a Grant-in-Aid for Scientific Research (C) from Japan Society for the Promotion of Science, and by the Spanish CICYT under contract BFM2000-1468.

Appendix A. Short-wavelength instability for $\alpha \gg 1$

When the streamwise wavelength of the perturbation is short compared with the spanwise length scale of the corrugation, the η-derivatives can be neglected, and (2.14) may be rewritten as

$$\left(\frac{\partial^2}{\partial \xi^2} - \alpha^2 J^{-1}\right)\widetilde{\phi} = 0. \tag{A 1}$$

Since the Jacobian $J(\xi, \eta)$ in (2.11) is not negative, we can write the solution as a WKB exponential expansion of the type

$$\widetilde{\phi}_0 = J^{1/4}\left\{A(\eta)\exp\left(+\alpha\int_{\xi_0}^{\xi} J^{-1/2}\,\mathrm{d}\xi\right) + B(\eta)\exp\left(-\alpha\int_{\xi_0}^{\xi} J^{-1/2}\,\mathrm{d}\xi\right)\right\}, \tag{A 2}$$

where $A(\eta)$ and $B(\eta)$ are smooth periodic functions. In order for the velocity to decay at $y \to -\infty$, i.e. $\zeta \to (2k+1)\pi$, the solution for $\xi < \xi_0$ should be

$$\widetilde{\phi}_0^- = A(\eta)J^{1/4}\exp\left(-\alpha\int_{\xi}^{\xi_0} J^{-1/2}\,\mathrm{d}\xi\right), \tag{A 3}$$

because $J^{-1/2} \to +\infty$ as $y \to -\infty$, while the solution for $\xi > \xi_0$ should be

$$\widetilde{\phi}_0^+ = B(\eta)J^{1/4}\exp\left(-\alpha\int_{\xi_0}^{\xi} J^{-1/2}\,\mathrm{d}\xi\right), \tag{A 4}$$

because $J^{-1/2} \to 1$ as $y \to \infty$. By substituting (A 3) and (A 4) into the matching conditions, (2.18) and (2.19), we have

$$(1-c_0)B(\eta) + (1+c_0)A(\eta) = 0, \tag{A 5}$$

$$-(1+c_0)B(\eta) + (1-c_0)A(\eta) = 0. \tag{A 6}$$

These equations determine the eigenvalues as

$$c_0 = \pm\mathrm{i}, \tag{A 7}$$

and the corresponding eigenvectors as

$$\frac{A}{B} = \pm\mathrm{i}, \tag{A 8}$$

both of which are independent of ξ_0 and α and coincide with those for the K–H instability of a flat vortex sheet.

Appendix B. Determination of the second-order corrections to the eigenvalues in the long-wave limit

The numerator and the denominator of the right-hand side of (4.12) can be expressed for the sinuous and for the varicose modes as follows. In the case of the sinuous mode, by using (2.12), (3.19), (3.20) and (4.2), we obtain

$$\int_0^{\infty} g_n\widetilde{\phi}_{0,n}\,\mathrm{d}\xi = \mathrm{e}^{-2n\xi_0}h_n^-\,I_n^- + \sinh^2 n\xi_0\,h_n^+ I_n^+, \tag{B 1}$$

where

$$h_n^- = 1 - 2\mathrm{e}^{-2n\xi_0} + \mathrm{e}^{-4n\xi_0} - 2\mathrm{e}^{-2n\xi_0}\sinh 2n\xi_0 - \mathrm{i}\,2^{5/2}\mathrm{e}^{-2n\xi_0}\sinh^{1/2} 2n\xi_0 \sinh n\xi_0, \tag{B 2}$$

$$h_n^+ = 1 + 2\mathrm{e}^{-2n\xi_0} + \mathrm{e}^{-4n\xi_0} - 2\mathrm{e}^{-2n\xi_0}\sinh 2n\xi_0 + \mathrm{i}\,2^{5/2}\mathrm{e}^{-2n\xi_0}\sinh^{1/2} 2n\xi_0 \cosh n\xi_0, \tag{B 3}$$

and

$$I_n^- = \int_0^{\xi_0} \left(1 + 2\frac{\mathrm{e}^{-\xi}}{\sinh\xi} - 2\frac{\mathrm{e}^{-2n\xi}}{\tanh\xi}\right) \sinh^2 n\xi \ \mathrm{d}\xi, \tag{B 4}$$

$$I_n^+ = \int_{\xi_0}^{\infty} \left(1 + 2\frac{\mathrm{e}^{-\xi}}{\sinh\xi} - 2\frac{\mathrm{e}^{-2n\xi}}{\tanh\xi}\right) \mathrm{e}^{-2n\xi} \ \mathrm{d}\xi. \tag{B 5}$$

The integrals (B 4) and (B 5) can be evaluated analytically. For example, we have, for the fundamental mode $n = 1$,

$$I_1^- = -\tfrac{3}{8} + \tfrac{1}{2}\cosh 2\xi_0 - \tfrac{1}{4}\sinh 2\xi_0 - \tfrac{1}{8}\mathrm{e}^{-4\xi_0}, \tag{B 6}$$

$$I_1^+ = \tfrac{1}{2}\mathrm{e}^{-2\xi_0} + \tfrac{1}{2}\mathrm{e}^{-4\xi_0}. \tag{B 7}$$

By use of (3.19) and (3.20), on the other hand, we have

$$\frac{4}{1-c_0^2}\widetilde{\phi}_{0,n}^+ \frac{\mathrm{d}\widetilde{\phi}_{0,n}^+}{\mathrm{d}\xi}\bigg|_{\xi=\xi_0} = -\mathrm{i}\,2^{3/2} n\,\mathrm{e}^{-2n\xi_0} \sinh^{1/2} 2n\xi_0 \sinh n\xi_0. \tag{B 8}$$

In the case of the varicose mode, by using (2.12), (3.22), (3.23) and (4.5), we obtain

$$\int_0^{\infty} g_n \widetilde{\phi}_{0,n}\,\mathrm{d}\xi = \mathrm{e}^{-2n\xi_0} h_n^- I_n^- + \cosh^2 n\xi_0\, h_n^+ I_n^+, \tag{B 9}$$

where

$$h_n^- = 1 + 2\mathrm{e}^{-2n\xi_0} + \mathrm{e}^{-4n\xi_0} - 2\mathrm{e}^{-2n\xi_0}\sinh 2n\xi_0 - \mathrm{i}\,2^{5/2}\mathrm{e}^{-2n\xi_0}\sinh^{1/2} 2n\xi_0 \cosh n\xi_0, \tag{B 10}$$

$$h_n^+ = 1 - 2\mathrm{e}^{-2n\xi_0} + \mathrm{e}^{-4n\xi_0} - 2\mathrm{e}^{-2n\xi_0}\sinh 2n\xi_0 + \mathrm{i}\,2^{5/2}\mathrm{e}^{-2n\xi_0}\sinh^{1/2} 2n\xi_0 \sinh n\xi_0, \tag{B 11}$$

and

$$I_n^- = \int_0^{\xi_0} \left\{\left(1 + 2\frac{\mathrm{e}^{-\xi}}{\sinh\xi} + 2\frac{\mathrm{e}^{-2n\xi}}{\tanh\xi}\right)\cosh n\xi - 4\frac{\mathrm{e}^{-n\xi}}{\tanh\xi}\right\}\cosh n\xi \ \mathrm{d}\xi, \tag{B 12}$$

$$I_n^+ = \int_{\xi_0}^{\infty} \left(1 + 2\frac{\mathrm{e}^{-\xi}}{\sinh\xi} + 2\frac{\mathrm{e}^{-2n\xi}}{\tanh\xi} - 4\frac{\mathrm{e}^{-n\xi_0}}{\cosh n\xi_0 \tanh\xi}\right)\mathrm{e}^{-2n\xi} \ \mathrm{d}\xi. \tag{B 13}$$

By use of (3.22) and (3.23), we have

$$\frac{4}{1-c_0^2}\widetilde{\phi}_{0,n}^+ \frac{\mathrm{d}\widetilde{\phi}_{0,n}^+}{\mathrm{d}\xi}\bigg|_{\xi=\xi_0} = -\mathrm{i}\,2^{3/2} n\,\mathrm{e}^{-2n\xi_0} \sinh^{1/2} 2n\xi_0 \cosh n\xi_0. \tag{B 14}$$

The corrections for the wall-bounded mapping (3.31) are computed in a similar way, using the corresponding eigenfunctions and Jacobian. The coefficients of the Fourier expansion (2.12) cannot in this case be easily expressed in closed form, although simple formulas can be found for some particular orders. Those needed for the computation of the corrections to the $n = 1$ eigenvalue are given below for reference:

$$\left.\begin{aligned} j_0 &= \frac{\sinh 2a}{2\sinh(a+\xi)\sinh(a-\xi)}, \\ j_1 &= \frac{2\sinh a\cosh\xi}{\sinh(a+\xi)\sinh(a-\xi)}, \\ j_2 &= -4\mathrm{e}^{-a}\sinh a + \frac{\sinh 2a}{\sinh(a+\xi)\sinh(a-\xi)}. \end{aligned}\right\} \tag{B 15}$$

Appendix C. Numerical computation of the eigenvalues for finite α

We consider solutions to equation (2.14) for finite α. When we write the sinuous velocity potential, which is an odd function with respect to $\eta = 2k\pi$, as

$$\widetilde{\phi}^{\pm} = \sum_{m=1}^{\infty} \widetilde{\phi}^{\pm}_m(\xi) \sin m\eta \tag{C 1}$$

and substitute (C 1) into (2.14), we have

$$\left(\frac{\mathrm{d}^2}{\mathrm{d}\xi^2} - m^2\right) \widetilde{\phi}^{\pm}_m - \alpha^2 f^{\pm}_m = 0, \tag{C 2}$$

where

$$f^{\pm}_m(\xi) = \tfrac{1}{2} j_0 \widetilde{\phi}^{\pm}_m + \tfrac{1}{2} \sum_{k=1}^{\infty} (j_{|m-k|} - j_{m+k}) \widetilde{\phi}^{\pm}_k. \tag{C 3}$$

From (2.18) and (2.19), the matching conditions to be imposed are

$$(1-c)\widetilde{\phi}^{+}_m + (1+c)\widetilde{\phi}^{-}_m = 0 \quad \text{on } \xi = \xi_0, \tag{C 4}$$

and

$$(1+c)\frac{\mathrm{d}\widetilde{\phi}^{+}_m}{\mathrm{d}\xi} + (1-c)\frac{\mathrm{d}\widetilde{\phi}^{-}_m}{\mathrm{d}\xi} = 0 \quad \text{on } \xi = \xi_0. \tag{C 5}$$

The boundary condition at $\xi = 0$ is

$$\widetilde{\phi}^{-}_m = 0, \tag{C 6}$$

which ensures the regularity of the velocity at $(\xi, \eta) = (0, 2k\pi)$, and the decay of the velocity at $y = -\infty$, i.e. $(\xi, \eta) = (0, (2k+1)\pi)$. For large ξ, on the other hand, $J^{-1} \approx 1$ and thus $f^{+}_m \approx \widetilde{\phi}^{+}_m$, so that (C 2) may be rewritten as

$$\left(\frac{\mathrm{d}^2}{\mathrm{d}\xi^2} - m^2 - \alpha^2\right) \widetilde{\phi}^{+}_m = 0. \tag{C 7}$$

Equation (C 7) has a solution, which decays at $\xi \to \infty$

$$\widetilde{\phi}^{+}_m \propto \exp(-\sqrt{m^2+\alpha^2}\,\xi). \tag{C 8}$$

Therefore, we consider the finite domain $\xi \in (0, 2\pi)$, and the boundary condition

$$\left(\frac{\mathrm{d}}{\mathrm{d}\xi} + \sqrt{m^2+\alpha^2}\right) \widetilde{\phi}^{+}_m = 0 \tag{C 9}$$

is imposed at $\xi = 2\pi$ to match the numerical solution with the analytical one (C 8).

We numerically solve the eigenvalue problem, (C 2)–(C 6) and (C 9) by using a fourth-order finite difference in the ξ-coordinate. For the case of $\xi_0 = \frac{1}{3}\pi$, the numerical computation is carried out with 61 uniform grid points in ξ (grid spacing is 0.105) and 50 Fourier modes in η.

REFERENCES

Acarlar, M. S. & Smith, C. R. 1987 A study of hairpin vortices in a laminar boundary layer. Part 2. Hairpin vortices generated by fluid injection. *J. Fluid Mech.* **175**, 43–83.

Asai, M., Minagawa, M. & Nishioka, M. 2002 The instability and breakdown of a near-wall low-speed streak. *J. Fluid Mech.* **455**, 289–314.

Bakewell, H. P. & Lumley, J. L. 1967 Viscous sublayer and adjacent wall region in turbulent pipe flow. *Phys. Fluids* **10**, 1880–1889.

Brooke, J. W. & Hanratty, T. J. 1993 Origin of turbulence-producing eddies in a channel flow. *Phys. Fluids* A **5**, 1011–1021.

Cowley, S. J., Baker, G. R. & Tanveer, S. 1999 On the formation of Moore curvature singularities in a vortex sheet. *J. Fluid Mech.* **378**, 233–267.

Crighton, D. G. 1973 Instability of an elliptic jet. *J. Fluid Mech.* **59**, 665–672.

Hall, P. & Horseman, N. J. 1991 The linear inviscid secondary instability of longitudinal vortex structures in boundary layers. *J. Fluid Mech.* **232**, 357–375.

Hamilton, J. M., Kim, J. & Waleffe, F. 1995 Regeneration mechanisms of near-wall turbulence structures. *J. Fluid Mech.* **287**, 317–348.

Hocking, L. M. 1964 The instability of a non-uniform vortex sheet. *J. Fluid Mech.* **18**, 177–186.

Itano, T. & Toh, S. 2001 The dynamics of bursting process in wall turbulence. *J. Phys. Soc. Japan* **70**, 701–714.

Jeong, J., Hussain, F., Schoppa, W. & Kim, J. 1997 Coherent structures near the wall in a turbulent channel flow. *J. Fluid Mech.* **332**, 185–214.

Jiménez, J. 1994 On the structure and control of near-wall turbulence. *Phys. Fluids* **6**, 944–953.

Jiménez, J. & Moin, P. 1991 The minimal flow unit in near-wall turbulence. *J. Fluid Mech.* **225**, 213–240.

Jiménez, J. & Pinelli, A. 1999 The autonomous cycle of near-wall turbulence. *J. Fluid Mech.* **389**, 335–359.

Jiménez, J. & Simens, M. P. 2001 Low-dimensional dynamics in a turbulent wall flow. *J. Fluid Mech.* **435**, 81–91.

Kawahara, G., Jiménez, J., Uhlmann, M. & Pinelli, A. 1998 The instability of streaks in near-wall turbulence. *CTR Annu. Res. Briefs, Stanford University*, pp. 155–170.

Kawahara, G. & Kida, S. 2001 Periodic motion embedded in plane Couette turbulence: regeneration cycle and burst. *J. Fluid Mech.* **449**, 291–300.

Kim, H. T., Kline, S. J. & Reynolds, W. C. 1971 The production of turbulence near a smooth wall in a turbulent boundary layers. *J. Fluid Mech.* **50**, 133–160.

Kim, J., Moin, P. & Moser, R. 1987 Turbulence statistics in a fully developed channel flow at low Reynolds number. *J. Fluid Mech.* **177**, 133–166.

Kline, S. J., Reynolds, W. C., Schraub, F. A. & Runstadler, P. W. 1967 The structure of turbulent boundary layers. *J. Fluid Mech.* **30**, 741–773.

Lasheras, J. C. & Choi, H. 1988 Three-dimensional instability of a plane free shear layer: an experimental study of the formation and evolution of streamwise vortices. *J. Fluid Mech.* **189**, 53–86.

Moore, D. W. 1979 The spontaneous appearance of a singularity in the shape of an evolving vortex sheet. *Proc. R. Soc. Lond.* A **365**, 105–119.

Nagata, M. 1990 Three-dimensional finite-amplitude solutions in plane Couette flow: bifurcation from infinity. *J. Fluid Mech.* **217**, 519–527.

Orlandi, P. & Jiménez, J. 1994 On the generation of turbulent wall friction. *Phys. Fluids* **6**, 634–641.

Panton, R. (Ed.) 1997 *Self-Sustaining Mechanisms of Wall Turbulence*. Computational Mechanics Publications.

Rayleigh, Lord 1879 On the instability of jets. *Proc. Lond. Math. Soc.* **10**, 4–13.

Reddy, S. C., Schmid, P. J., Baggett, J. S. & Henningson, D. S. 1998 On stability of streamwise streaks and transition thresholds in plane channel flows. *J. Fluid Mech.* **365**, 269–303.

Saffman, P. G. 1992 *Vortex Dynamics*. Cambridge University Press.

Saxena, V., Leibovich, S. & Berkooz, G. 1999 Enhancement of three-dimensional instability of free shear layers. *J. Fluid Mech.* **379**, 23–38.

Schoppa, W. 2000 Studies of coherent structure generation in near-wall turbulence. PhD disseration, University of Houston.

Schoppa, W. & Hussain, F. 1997 Genesis and dynamics of coherent structures in near-wall turbulence: A new look. In *Self-Sustaining Mechanisms of Wall Turbulence* (ed. R. Panton), pp. 385–422. Computational Mechanics Publications.

Schoppa, W. & Hussain, F. 1998 Formation of near-wall streamwise vortices by streak instability. *AIAA Paper* 98-3000.

Schoppa, W. & Hussain, F. 2002 Coherent structure generation in near-wall turbulence. *J. Fluid Mech.* **453**, 57–108.

Schoppa, W., Hussain, F. & Metcalfe, R. W. 1995 A new mechanism of small-scale transition in a plane mixing layer: core dynamics of spanwise vortices. *J. Fluid Mech.* **298**, 23–80.

Sreenivasan, K. R. 1988 A unified view of the origin and morphology of the turbulent boundary layer structure. In *Proc. IUTAM Symp. on Turbulence Management and Relaminarisation* (ed. H. W. Liepmann & R. Narasimha), pp. 37–61. Springer.

Stretch, D. 1990 Automated pattern eduction from turbulent flow diagnostics. *CTR Annu. Res. Briefs, Stanford University*, pp. 145–157.

Swearingen, J. D. & Blackwelder, R. F. 1987 The growth and breakdown of streamwise vortices in the presence of a wall. *J. Fluid Mech.* **182**, 255–290.

Toh, S. & Itano, T. 1999 Low-dimensional dynamics embedded in a plane Poiseuille flow turbulence. Traveling-wave solution is a saddle point? Preprint. arXiv.org e-Print Archive, http://xxx.lanl.gov/abs/physics/9905012.

Toh, S. & Itano, T. 2001 On the regeneration mechanism of turbulence in the channel flow – role of the traveling-wave solution. In *Proc. IUTAM Symp. on Geometry and Statistics of Turbulence* (ed. T. Kambe, T. Nakano & T. Miyauchi), pp. 305–310. Kluwer.

Waleffe, F. 1995 Hydrodynamic stability and turbulence: Beyond transients to a self-sustaining process. *Stud. Appl. Maths* **95**, 319–343.

Waleffe, F. 1997 On a self-sustaining process in shear flows. *Phys. Fluids* **9**, 883–900.

Waleffe, F. 1998 Three-dimensional coherent states in plane shear flows. *Phys. Rev. Lett.* **81**, 4140–4143.

Waleffe, F. 2001 Exact coherent structure in channel flow. *J. Fluid Mech.* **435**, 93–102.

Waleffe, F. & Kim, J. 1997 How streamwise rolls and streaks self-sustain in a shear flow. In *Self-Sustaining Mechanisms of Wall Turbulence* (ed. R. Panton), pp. 309–332. Computational Mechanics Publications.